Terahertz charge dynamics unveil fundamental transport anisotropy in charge-ordered $Pr_{0.5}Eu_{0.5}NiO_3$ nickelate thin films

Sarmistha Das, G. L. Prajapati, P. Anagha, and D. S. Rana*
Department of Physics, Indian Institute of Science Education and Research, Bhopal, 462066, India

(Received 18 April 2018; revised manuscript received 12 July 2018; published 6 September 2018)

Electrons condensed in a collective mode and behaving as free charge carriers are two important facets induced by the complex intertwining of charge, spin, orbital, and lattice degrees of freedom. Existence of these two electronic ground states in the same structural/chemical phase is as much desired as it is elusive in complex oxides. Using some unique attributes of terahertz (THz) spectroscopy, we show existence of two fundamentally different electronic phenomena in $Pr_{0.5}Eu_{0.5}NiO_3$ nickelate in the same structural phase but along two orthogonal in-plane axes [001] and [1$\bar{1}$0] of thin films. While a collective response of charge via charge-density-wave type excitation manifests along the [001] direction, an entirely different Drude-Smith type free carrier response manifests along the other in-plane orthogonal axis. This anisotropy, on one hand, unveils the strain engineered crystallographic preferences of the underlying charge-ordering phenomenon; on the other hand, the different conduction channels open up possibilities of application of nickelates such as in THz transmission modulators.

DOI: 10.1103/PhysRevB.98.115110

The complex perovskite oxides display vast variety of electronic and magnetic ground states emerging from the concurrent ordering of different degrees of freedom. The charge carrier transport in such materials is a result of several spontaneous symmetry breaking transitions. High-temperature superconductivity, metal-insulator transition (MIT), colossal magnetoresistance, magnetoelectric effect, etc., [1–3] are some of such unconventional ground states. In this context, the unusual electronic properties of rare-earth nickelates [$RNiO_3$ (R = rare earth)] have recently been a recurrent research theme owing to both fundamental and applied aspects. Apart from the electron correlations, a crossover from localized to itinerant electronic behavior associated with complex magnetic and structural transition, and the competition between Mott and charge-transfer electronic phases are of fundamental interest, while tuning and controlling these properties via subtle structural modulations to suit oxide electronics is of technological interest [4–6]. These nickelates also offer a platform to study the canonical MIT in the light of electron-phonon interaction as observed in systems with Peierl's transition and superconducting phase [7,8].

The transition from localized to itinerant electronic state in nickelates via controlling temperature, pressure, chemical doping, epitaxial strain, etc., is attributed to the changing of electronic volume with the change in average R-cation size and concomitant modification of the charge-orbital ordered ground state [3,5,9–11]. The phase-diagram of nickelates reveals that the degree of lattice distortion keeps on increasing with decreasing R-cation size. Here, $EuNiO_3$ (cation radius of Eu = 1.12 Å) possesses one of the highest distorted structures that can be formed in thin film motif. The $PrNiO_3$ (cation radius of Pr = 1.179 Å), in contrast, lies close to least distorted member $LaNiO_3$, yet exhibits concomitant MIT and magnetic order [3]. Mixing these two structures in the form of $Pr_{0.5}Eu_{0.5}NiO_3$ (PENO) can induce reasonable level of lattice distortion, in which the presence of quenched disorder (due to cation size mismatch at the R site) can also play a role in modification of physical properties [12–14]. The resultant distortion and disorder can be magnified by imposing different levels of biaxial epitaxial strain which is considered an efficient way to manipulate the directional ordered state. In this context, the two dissimilar in-plane epitaxial strains can potentially lead to the manifestation of axial anisotropy [15,16].

While investigations of anisotropic properties have been carried out on other popular manganite and cuprate systems, such studies on nickelate systems have remained elusive so far. Besides, the study of anisotropy offers a multifunctional utility: prospects of a material in which several coexisting phases can be obtained as well as be manipulated by external stimuli. Also, the anisotropic materials are more desirable for engineering spintronic devices. The dc transport data usually cannot unveil fundamental anisotropy in such complex systems as it fails to probe the low energy mode of collective charge dynamics. Kida and Tonouchi pioneered the use of THz time-domain spectroscopy (THz-TDS) for probing the charge density wave (CDW) mode in manganites or in any class of complex oxides [17,18]. This led to extensive use of THz spectroscopy for resolving various issues including anisotropy of the charge order and the CDW in manganites. In nickelates, the charge order and the CDW exist in the prototypical $NdNiO_3$ system. However, searches for such low energy modes extending to other members and investigations on the transport anisotropy are still lacking. Here, we have carried out detailed investigations on the anisotropic properties on PENO nickelate employing THz spectroscopy. We demonstrate manifestation of CDW type *collective dynamic transport* phenomena along one crystal axis and a contrasting *free carrier transport* along the other crystal axis. The anisotropic CDW-type modulation was obtained by performing THz-TDS studies on PENO thin

*dsrana@iiserb.ac.in

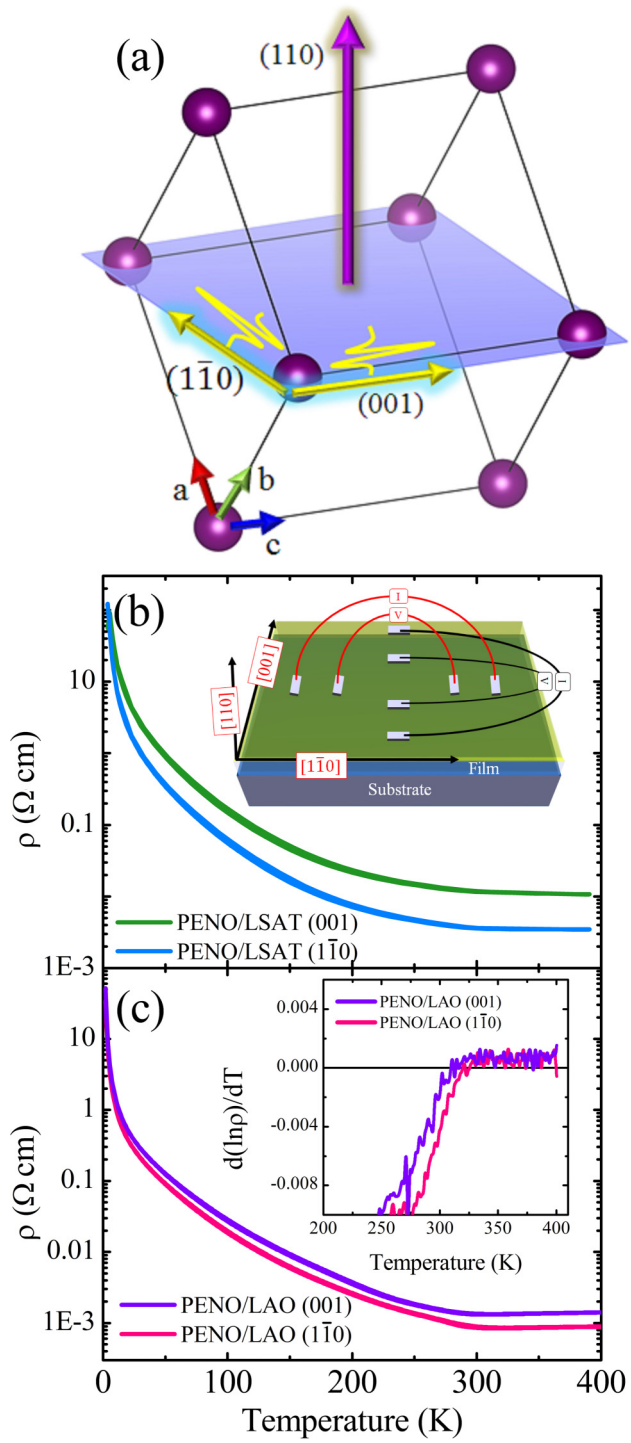

FIG. 1. (a) Schematic representation of PENO thin film, grown along the (110) direction, showing two different sets of THz-TDS data collected as the polarized THz pulse transmitted through (1$\bar{1}$0) and (001) directions. The ρ-T profiles of (b) PENO/LSAT and (c) PENO/LAO films along (001) and (1$\bar{1}$0) directions. The inset in (b) depicts the four-probe measurement setup along two different in-plane orthogonal axes and the inset in (c) shows the $d(\ln \rho)/dT$ profiles.

films deposited on $(LaAlO_3)_{0.3}(Sr_2TaAlO_6)_{0.7}$ (LSAT) (110) and $LaAlO_3$ (LAO) (110) substrates in which two in-plane axes belong to different families of (110) and (100) crystal axes. Figure 1(a) represents the schematic of measurement procedure. The LAO and LSAT with (110) orientation were chosen to induce compressive and tensile strain, respectively, along with the opportunity to study the effect of biaxial in-plane anisotropic strain. These studies were performed in the frequency range of 0.2–1.5 THz and a temperature range of 30–300 K.

The experimental details of film synthesis and their characterization are given in the Supplemental Material [19]. The θ–2θ XRD patterns of the PENO thin films on LSAT(110) [PENO/LSAT] and LAO(110) [PENO/LAO] substrates depict that both the films are phase pure and epitaxial (Fig. S1 [19]). The film peaks at higher 2θ angles than that of the substrate for PENO/LSAT and at lower 2θ value for PENO/LAO suggest tensile and compressive strain, respectively. The in-plane axes of these films ([1$\bar{1}$0] and [001]) are determined by reciprocal space mapping (RSM) measurements (Figs. S2 and S3 [19]). The (110) oriented LSAT substrate has two completely different orthogonal in-plane crystal planes ($a_{(001)} \sim 3.868$ Å and $a_{(1\bar{1}0)} \sim 5.470$ Å). Similarly, for LAO (110) substrate, the in-plane lattice parameters are $a_{(001)} \sim 3.794$ Å and $a_{(1\bar{1}0)} \sim 5.365$ Å. Accessibility to these two different planes in thin films allows one to explore the existence of anisotropy in various physical/optical properties. The detailed structural analysis reveals that the both film possess tetragonal symmetry (Figs. S2 and S3) [19–21].

The zero-field dc electrical resistivity (ρ) vs temperature (T) along two different in-plane directions for both films are plotted in Figs. 1(b) and 1(c). The inset of Fig. 1(b) shows the schematic for the four-probe arrangements to acquire ρ-T profiles along two different in-plane orthogonal directions of thin film. These data depict the insulating nature of the films along both in-plane directions for PENO/LSAT film. The PENO/LAO film, however, exhibits an MIT at ~309 and 319 K along (001) and (1$\bar{1}$0) directions, respectively, as determined from zero crossing on $d(\ln \rho)/dT$ plots [inset of Fig. 1(c)]. It may be seen that the resistivity profiles are similar across the two axes for both films. Overall, except for a small difference in magnitude, the resistivity does not show any qualitative difference or anisotropy across two different in-plane axes. In such a scenario, THz spectroscopy, having the attribute of frequency-dependent properties, may be useful for exploring the existence of anisotropy or multiple electronic ground states [22].

The THz low-energy charge dynamics along the two different in-plane directions of PENO/LSAT thin film are probed in the framework of the schematic shown in Fig. 1(a). The real part (σ_1) of THz complex optical conductivity (σ^*) as a function of THz frequency (f) (0.2–1.5 THz) is plotted in Figs. 2(a) and 2(b) for both orthogonal [001] and [1$\bar{1}$0] in-plane directions, respectively. The σ_1-f spectrum shows different behavior along the two different in-plane axes. Along the [001] direction, a pronounced peak-like resonance feature manifests in THz conductivity, while along the [1$\bar{1}$0] orientation the σ_1-f spectrum is clearly featureless. The CDW manifestation has been recognized previously through the resonant-like behavior of σ^* in meV energy range spectra. A collective CDW excitation mode in THz spectrum should possess certain features [17,18,23,24], namely, (i) the peak conductivities are observed to be of the order of 10^2–10^3 Ω cm, (ii) the peak conductivity follows the dispersive relation, i.e., the peak σ_1 is accompanied

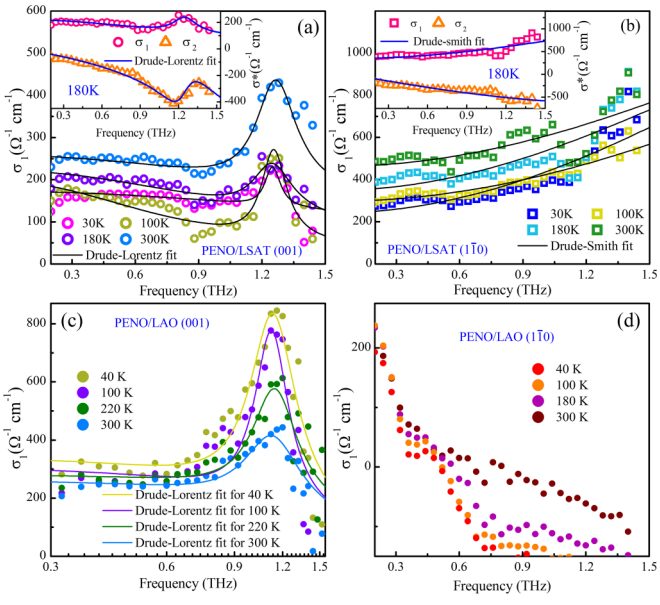

FIG. 2. σ_1-f plots of PENO/LSAT film, at various temperatures (a) along the (001) direction and (b) along (1$\bar{1}$0). The inset shows simultaneous (a) Drude-Lorentz fitted curves and (b) Drude-Smith fitted curve of σ_1 and σ_2 together at a constant temperature of 180 K. σ_1-f plots of PENO/LAO film, at various temperatures (c) along the (001) direction and (d) along the (1$\bar{1}$0) direction.

by a dip in the real part of the complex dielectric constant (ε_1), and (iii) the CDW phason mode is infrared active and falls in the energy range 1–6 meV. In the $\sigma_1^{(001)}$-f spectrum, the appearance of a peak around 1.25 THz (∼5 meV) for the entire temperature range seems to be a mode of low energy CDW-type excitation. The existence of dielectric dispersion, as noticed from a phase lag between $\varepsilon_1^{(001)}$ and $\sigma_1^{(001)}$, was observed for all the spectra, and is shown for 180 K in Fig. S4(a) which further verifies the authenticity of resonance absorption [19]. In the entire temperature range studied here, a dispersive response between the real and imaginary components [($\sigma_1^{(001)}$) and ($\sigma_2^{(001)}$)] of $\sigma^{*(001)}$ at the THz resonant frequency (∼1.25 THz) was observed. One such response at 180 K is plotted in the inset of Fig. 2(a). Another possibility of a polaronic peak is ruled out, as in nickelates the polaronic excitation occurs at an energy which is ∼5–6 times higher than that observed in the present case. [17–18,23–25].

The THz conductivity spectra along the [1$\bar{1}$0] direction, in contrast to that of (001), are featureless. Furthermore, as shown in Fig. S4(b) [19], no resonance-like signature was observed in temperature-dependent ($\varepsilon_1^{1\bar{1}0}$)-$f$ profiles, which also rules out the existence of any phase lag between ($\varepsilon_1{}^{1\bar{1}0}$) and $\sigma_1^{(1\bar{1}0)}$. However, a dip-like feature visible in ($\sigma_1^{1\bar{1}0}$)-f spectra at around 1.2 THz manifests only in high temperatures and lacks dielectric dispersion; therefore, it can't be assigned to a resonant absorption mode. The lack of any peak in $\sigma_1^{(1\bar{1}0)}$ at zero frequency rules out the free charge carriers' response as per the conventional Drude model. These two different types of non-Drude conductivity responses along two different in-plane directions need to be modeled in the scope of relevant conductivity models.

To analyze the resonant response of $\sigma^{*(001)}$, the Drude-Lorentz (DL) model was employed as expressed below [7,16]:

$$\sigma^*(\omega) = \frac{1}{4\pi}\left\{\frac{\tau_D\omega_p^2}{1-i\omega\tau_D} + \frac{S_L^2\omega}{\omega\tau_L + i\left(\omega_L^2-\omega^2\right)} - i\omega(\epsilon_\infty - 1)\right\}. \quad (1)$$

Here, the first term denotes the Drude contribution, where τ_D and ω_p signify Drude scattering rate and plasma frequency, respectively. The second term appears due to the Lorentz oscillator, which contributes a resonant effect at a finite resonant frequency of ω_L with oscillator strength of S_L and line width τ_L^{-1}. The ϵ_∞ signifies a value of dielectric constant in the frequency limit of infinity. We found that our measured $\sigma^{*(001)}$ follows the DL model, as the calculated and experimental data converge really well. All such data, plotted along with their respective fitted curves, are presented in Fig. 2(a). At 180 K, the $\sigma_1^{(001)}$ and $\sigma_2^{(001)}$ are plotted with their simultaneous DL fitted curve in the inset of Fig. 2(a) and their dispersive response also satisfies the DL model. The fitted values of ω_L lie in the vicinity of 1.25 THz for the entire temperature range of 5–300 K. For 180 K, we obtained $\omega_p \sim 0.27$ eV, $\tau_D \sim 0.68$ THz, $S_L \sim 66$ meV, and $\tau_L \sim 5.26$ THz.

Now we model the $\sigma^{*(1\bar{1}0)}$-f spectra to a well-known Drude-Smith (DS) model [26–28], expressed as

$$\sigma^* = \frac{1}{4\pi}\frac{\omega_p^2\tau_D}{1-i\omega\tau_D}\left[1+\sum_j \frac{c_j}{1-i\omega\tau_{\mathrm{DS}}}\right] - \frac{1}{4\pi}i\omega(\epsilon_\infty - 1). \quad (2)$$

Here, apart from Drude term, the additional term in the square brackets signifies the contributions of the back-scattered charge carriers. The j refers to the total number of collisions as encountered by the charge carriers and here, and c_j is the Drude-Smith coefficient, which defines the fraction of initial velocity of charge carriers after the jth superscript collision. Taking $j = 1$, only one scattering event was considered. We can define as $c_j \to c_1 \to c$, where c follows the condition $-1 \leqslant c \leqslant 0$. At a fixed temperature, $\sigma_1^{(1\bar{1}0)}$ and $\sigma_2^{(1\bar{1}0)}$ are fitted simultaneously to the DS model. Frequency-dependent $\sigma_1^{(1\bar{1}0)}$ at different temperatures are plotted along with their respective DS-fitted data [Fig. 2(b)]. At 180 K, the DS-fitted spectra of $\sigma_1^{(1\bar{1}0)}$ and $\sigma_2^{(1\bar{1}0)}$ are found to fit well with experimental data with $c = -0.89$ [inset of Fig. 2(b)]. This high negative c suggests the presence of disorder/scattering centers along the [1$\bar{1}$0] direction and also brings out the directional disordered nature in PENO thin film. The unidirectional manifestation of CDW along (001) can also be understood as a likely outcome of the anisotropic strain modulated directional nature of Ni e_g orbitals. Some basic relevant aspects of such anisotropy in PENO thin films—such as whether (i) this anisotropic behavior is intrinsic and/or driven by epitaxial strain, (ii) the observed CDW-like mode can sustain in another strained state, and (iii) such pronounced THz transport anisotropy has any relation with PENO being mixed R-site nickelate, in which disorder seems to prompt directional anisotropy—are discussed henceforth.

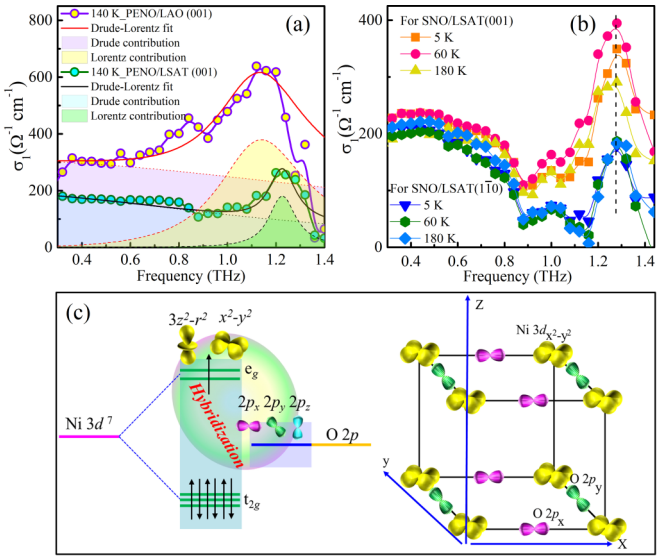

FIG. 3. (a) Drude and Lorentz contributions in σ_1 of PENO films at 140 K, grown on LAO(110) and LSAT(110) substrates. (b) σ_1-f plots of SNO film, grown on LSAT(110) substrate, at various temperatures along two different directions, (001) and (1$\bar{1}$0). (c) The schematic representation of Ni-3d and O-2p orbital arrangements near Fermi level. The two different colors of O-2p_x and O-2p_y symbolize having dissimilar occupancy, depending on the different level of hybridization, induced by biaxial anisotropic strain. For simplicity, Ni-3$d_{3z^2-r^2}$ and O-2p_z are not included here.

To address the strain related aspect, THz spectroscopy was performed on compressive PENO/LAO (110) ($a \sim 3.794$ Å) film. Here too, two different lattice parameters along the two in-plane directions are $a_{(001)} \sim 3.794$ Å and $a_{(1\bar{1}0)} \sim 5.365$ Å. The THz frequency-dependent optical responses at various temperatures for two different in-plane directions are shown in Figs. 2(c) and 2(d). In this case too, we observed a distinct anisotropic behavior. Along the (001) direction, the peak in ($\sigma_1^{(001)}$) at the vicinity of 1.12 THz seems possess all the features of a CDW-like mode [Fig. 2(c)]. Also, a phase lag between $\varepsilon_1^{(001)}$ and $\sigma_1^{(001)}$ is clearly observed, as plotted for 40 K in Fig. S5(a). These data too fit well with the DL model [Fig. 2(c)]. The $\sigma_1^{(1\bar{1}0)}$-f spectrum, in contrast, exhibits no such CDW peak-like feature at any temperature and no dispersion is observed in the $\varepsilon_1^{(1\bar{1}0)}$-$f$ profile [Figs. 2(d) and S5(b)] [19].

To compare the CDW-like resonant excitations of two differently strained PENO thin films, we have plotted $\sigma_1^{(001)}$ for PENO/LSAT and PENO/LAO thin films at 140 K along with their respective DL fitted curve [Fig. 3(a)]. Here, we observe that both the Drude and the Lorentz spectral weights of PENO/LAO are higher than that of PENO/LSAT. Additionally, the oscillator strength of PENO/LAO is nearly double that of PENO/LSAT. However, for both cases, the anisotropic nature of THz conductivity is qualitatively the same, as the CDW-like manifestation has axial dependence. This unambiguously suggests that the transport anisotropy of PENO is intrinsic and does not depend on the epitaxial strain. In contrast to this, a previous study of $NdNiO_3$ thin film on LAO(110) exhibits clearly opposite behavior, as in that case the THz CDW peak manifested along both in-plane axes [7]. The comparison of PENO with reported $NdNiO_3$ results suggests that the anisotropic transport does not manifest in pure systems. To lend more credence, we studied $SmNiO_3$ (SNO) thin film, which exhibits MIT at around 400 K. A comparison of PENO with SNO is highly appropriate as both these systems have same average cation size at the R site. At all temperatures, we observed a CDW peak for SNO thin film on LSAT(110) substrate and further found that CDW-like manifests at the same frequency along both in-plane axes (albeit with some difference in σ_1) [Fig. 3(b)], as was the case of $NdNiO_3$ [7]. Hence, for R-site mixed nickelate PENO which has intrinsic cation disorder, the anisotropic strain seems effective to prompt a shear-mode distortion in NiO_6 octahedra, which induces axial dependence of conductivity phenomena.

Overall, for PENO thin films, the observed anisotropy seems to be hosted by the intrinsic complex nature of the material. This is because the quenching of CDW-like resonance is a predominant control of R-cation size for rare-earth nickelates [7,12,27,29]. In this context, for the sample with finite cation disorder, local distribution of strain may occur due to the anisotropic lattice mismatch/strain, which can modulate the coupling between electronic and elastic degrees of freedom [30–32]. This may have further strongly influenced directional-dependent hybridization of O-2p with Ni-3d orbitals. As a result, the orbital occupancies of O-2p_x and O-2p_y become different, which might induce anisotropic conductivity in the system [Fig. 3(c)] [33,34]. A very similar mechanism was observed in manganite films, for which the strain-dependent anisotropy is attributed to the modified hybridization of O-2p with Mn-3d orbitals [33]. In the present study, the anisotropic properties of PENO are unaffected by the nature of epitaxial strain but seem to be induced by cation disorder at the R site. Overall, the intrinsic anisotropic nature of PENO thin films can be attributed to (i) anisotropic strain derived seeding and growth of electronic conduction channel along a preferential direction, (ii) directional properties of the Ni e_g orbital, (iii) the possibility of anisotropic variation of electron occupancy between two different in-plane O-2p states, i.e., O-2p_x and 2p_y [Fig. 3(c)] [33,34], and (iv) directional variation in inter-chain coupling of adjacent CDWs in PENO thin film which is epitaxially locked with anisotropic strain, induced by the substrate [33–35].

To conclude, two different crystal axes of both tensile and compressive strained PENO thin films were excited by a THz electric field. While well-defined collective carrier dynamics in the form of a CDW-like resonance peak manifested along the (001) direction under both the strained states, a completely different mechanism of free THz carrier dynamics in the form of modified free carrier conductivity appeared along the other orthogonal (1$\bar{1}$0) direction for both the cases. Such strong low energy transport anisotropy occurring in two different strained states clearly suggests the observed effects to be intrinsic in nature. This is spontaneous attribution of anisotropic strain modulated shear-mode distortion in NiO_6 octahedra, triggered by the directional properties of Ni-e_g orbitals and occupancy of O-2p states. Such intrinsic anisotropic properties of correlated systems have rarely been observed and can be an intrinsic source of two conduction channels for THz frequency modulators/filters.

D.S.R. thanks the Science and Engineering Research Board (SERB), Department of Science and Technology (DST), New Delhi, for financial support under EMR Grant No. EMR/2016/003598. Financial support from DST-FIST program is also thankfully acknowledged.

[1] E. Dagotto, T. Hotta, and A. Moreo, Phys. Rep. **344**, 1 (2001).
[2] S. Cox, J. Singleton, R. D. McDonald, A. Migliori, and P. B. Littlewood, Nat. Mater. **7**, 25 (2008).
[3] S. Middey, J. Chakhalian, P. Mahadevan, J. W. Freeland, A. J. Millis, and D. D. Sarma, Annu. Rev. Mater. Res. **46**, 305 (2016).
[4] J. B. Torrance, P. Lacorre, A. I. Nazzal, E. J. Ansaldo, and C. Niedermayer, Phys. Rev. B **45**, 8209 (1992).
[5] Z. He and A. J. Millis, Phys. Rev. B **91**, 195138 (2015).
[6] J. W. Freeland, M. van Veenendaal, and J. Chakhalian, J. Electron Spectrosc. Relat. Phenom. **208**, 56 (2016).
[7] R. Rana, P. Pandey, V. E. Phanindra, S. S. Prabhu, and D. S. Rana, Phys. Rev. B **97**, 045123 (2018).
[8] S. B. Lee, R. Chen, and L. Balents, Phys. Rev. Lett. **106**, 016405 (2011).
[9] P.-H. Xiang, N. Zhong, C.-G. Duan, X. D. Tang, Z. G. Hu, P. X. Yang, Z. Q. Zhu, and J. H. Chu, J. Appl. Phys. **114**, 243713 (2013).
[10] P. C. Canfield, J. D. Thompson, S.-W. Cheong, and L. W. Rupp, Phys. Rev. B **47**, 12357 (1993).
[11] B. Lau and A. J. Millis, Phys. Rev. Lett. **110**, 126404 (2013).
[12] S. Das, V. E. Phanindra, S. S. Philip, and D. S. Rana, Phys. Rev. B **96**, 144411 (2017).
[13] L. M. Rodriguez-Martinez and J. P. Attfield, Phys. Rev. B **54**, R15622(R) (1996).
[14] J. P. Attfield, A. L. Kharlanov, and J. A. McAllister, Nature (London) **394**, 157 (1998).
[15] M. Liu, Q. Zou, C. Ma, G. Collins, S.-B. Mi, C.-L. Jia, H. Guo, H. Gao, and C. Chen, ACS Appl. Mater. Interfaces **6**, 8526 (2014).
[16] R. Rana, P. Pandey, D. S. Rana, K. R. Mavani, I. Kawayama, H. Murakami, and M. Tonouchi, Phys. Rev. B **87**, 224421 (2013).
[17] N. Kida and M. Tonouchi, Phys. Rev. B **66**, 024401 (2002).
[18] J. Fujioka, Y. Ida, Y. Takahashi, N. Kida, R. Shimano, and Y. Tokura, Phys. Rev. B **82**, 140409(R) (2010).
[19] See Supplemental Material at http://link.aps.org/supplemental/10.1103/PhysRevB.98.115110 for experimental details, structural analysis, and optical properties of the PENO films.
[20] Z. Yin, Z. Huang, G. Gao, W. Wu, G. Wang, and Y. Wang, J. Phys. D **42**, 062004 (2009).
[21] E. Guo, R. Roth, A. Herklotz, D. Hesse, and K. Dörr, Adv. Mater. **27**, 1615 (2015).
[22] V. E. Phanindra, P. Agarwal, and D. S. Rana, J. Phys. Condens. Matter **29**, 445604 (2017).
[23] R. Rana, D. S. Rana, K. R. Mavani, I. Kawayama, H. Murakami, and M. Tonouchi, Appl. Phys. Lett. **101**, 252401 (2012).
[24] M. Karttunen, M. Haataja, K. R. Elder, and M. Grant, Phys. Rev. Lett. **83**, 3518 (1999).
[25] M. A. Mroginski, N. E. Massa, H. Salva, J. A. Alonso, and M. J. Martinez-Lope, Phys. Rev. B **60**, 5304 (1999).
[26] S. Das, V. E. Phanindra, K. S. Kumar, P. Agarwal, K. C. Dhaker, and D. S. Rana, J. Phys. Condens. Matter **29**, 025805 (2017).
[27] V. E. Phanindra, S. Das, K. S. Kumar, P. Agarwal, R. Rana, and D. S. Rana, Phys. Rev. B **95**, 085114 (2017).
[28] K. S. Kumar, S. Das, V. E. Phanindra, and D. S. Rana, J. Phys. D **50**, 505303 (2017).
[29] H. Park, A. J. Millis, and C. A. Marianetti, Phys. Rev. Lett. **109**, 156402 (2012).
[30] C. Ma, D. Han, M. Liu, G. Collins, H. Wang, X. Xu, Y. Lin, J. Jiang, S. Zhang, and C. Chen, Sci. Rep. **6**, 37337 (2016).
[31] T. Z. Ward, J. D. Budai, Z. Gai, J. Z. Tischler, L. Yin, and J. Shen, Nat. Phys. **5**, 885 (2009).
[32] K. H. Ahn, T. Lookman, and A. R. Bishop, Nature (London) **428**, 401 (2004).
[33] B. Wang, L. You, P. Ren, X. Yin, Y. Peng, B. Xia, L. Wang, X. Yu, S. M. Poh, P. Yang, G. Yuan, L. Chen, A. Rusydi, and J. Wang, Nat. Commun. **4**, 2778 (2013).
[34] M. H. Upton, Y. Choi, H. Park, J. Liu, D. Meyers, J. Chakhalian, S. Middey, J.-W. Kim, and P. J. Ryan, Phys. Rev. Lett. **115**, 036401 (2015).
[35] K. Inagaki, T. Matsuura, M. Tsubota, S. Uji, T. Honma, and S. Tanda, Phys. Rev. B **93**, 075423 (2016).